

# Active fiber-based retroreflector providing phase-retracing anti-parallel laser beams for precision spectroscopy

A. BEYER,<sup>1,\*</sup> L. MAISENBACHER,<sup>1</sup> A. MATVEEV,<sup>1</sup> R. POHL,<sup>1,2</sup>  
K. Khabarova,<sup>3,4</sup> Y. CHANG,<sup>1</sup> A. GRININ,<sup>1</sup> T. LAMOUR,<sup>1</sup>  
T. SHI,<sup>1</sup> D. C. YOST,<sup>1,5</sup> TH. UDEM,<sup>1,6</sup> T. W. HÄNSCH,<sup>1,6</sup>  
AND N. KOLACHEVSKY<sup>3,4</sup>

<sup>1</sup> Max-Planck-Institut für Quantenoptik, 85748 Garching, Germany

<sup>2</sup> Now at: Johannes Gutenberg-Universität Mainz, Germany

<sup>3</sup> On leave from: P.N. Lebedev Physical Institute, 119991 Moscow, Russia

<sup>4</sup> Also at: Russian Quantum Center, 143025 Skolkovo, Russia

<sup>5</sup> Now at: Colorado State University, Fort Collins, USA

<sup>6</sup> Ludwig-Maximilians-Universität, München, Germany

\* Axel.Beyer@mpq.mpg.de

**Abstract:** We present an active fiber-based retroreflector providing high quality phase-retracing anti-parallel Gaussian laser beams for precision spectroscopy of Doppler sensitive transitions. Our design is well-suited for a number of applications where implementing optical cavities is technically challenging and corner cubes fail to match the demanded requirements, most importantly retracing wavefronts and preservation of the laser polarization. To illustrate the performance of the system, we use it for spectroscopy of the 2S-4P transition in atomic hydrogen and demonstrate an average suppression of the first order Doppler shift to 4 parts in  $10^6$  of the full collinear shift. This high degree of cancellation combined with our cryogenic source of hydrogen atoms in the metastable 2S state is sufficient to enable determinations of the Rydberg constant and the proton charge radius with competitive uncertainties. Advantages over the usual Doppler cancellation based on corner cube type retroreflectors are discussed as well as an alternative method using a high finesse cavity.

© 2016 Optical Society of America

**OCIS codes:** (020.3690) Line shapes and shifts; (060.2350) Fiber optics imaging; (120.3930) Metrological instrumentation; (270.5580) Quantum electrodynamics; (300.6320) Spectroscopy, high-resolution; (300.6210) Spectroscopy, atomic.

## References and links

1. W. Demtröder, *Laser Spectroscopy*, Vol. 2 (Springer-Verlag, 2008).
2. A. Beyer, J. Alnis, K. Khabarova, A. Matveev, C. G. Parthey, D. C. Yost, R. Pohl, Th. Udem, T. W. Hänsch, and N. Kolachevsky, "Precision spectroscopy of the 2S-4P transition in atomic hydrogen on a cryogenic beam of optically excited 2S atoms," *Ann. Phys. (Berlin)* **525**, 671–679 (2013).
3. C. G. Parthey, A. Matveev, J. Alnis, B. Bernhardt, A. Beyer, R. Holzwarth, A. Maistrou, R. Pohl, K. Predehl, Th. Udem, T. Wilken, N. Kolachevsky, M. Abgrall, D. Rovera, Ch. Salomon, Ph. Laurent, and T. W. Hänsch, "Improved measurement of the hydrogen 1S-2S transition frequency," *Phys. Rev. Lett.* **107**, 203001 (2011).
4. R. Pohl, R. Gilman, G. A. Miller, and K. Pachucki, "Muonic hydrogen and the proton radius puzzle," *Annu. Rev. Nucl. Part. Sci.* **63**, 175–204 (2013).
5. A. Beyer, C. G. Parthey, N. Kolachevsky, J. Alnis, K. Khabarova, R. Pohl, E. Peters, D. C. Yost, A. Matveev, K. Predehl, S. Droste, T. Wilken, R. Holzwarth, T. W. Hänsch, M. Abgrall, D. Rovera, Ch. Salomon, Ph. Laurent, and Th. Udem, "Precision spectroscopy of atomic hydrogen," *J. Phys. Conf. Ser.* **467**, 012003 (2013).
6. D. J. Berkeland, E. A. Hinds, and M. G. Boshier, "Precise optical measurement of Lamb shifts in atomic hydrogen," *Phys. Rev. Lett.* **75**, 2470–2473 (1995).
7. R. C. Brown, S. Wu, J. V. Porto, C. J. Sansonetti, C. E. Simien, S. M. Brewer, J. N. Tan, and J. D. Gillaspay, "Quantum interference and light polarization effects in unresolvable atomic lines: Application to a precise measurement of the Li-6, Li-7 D-2 lines," *Phys. Rev. A* **87**, 032504 (2013).
8. See for instance HM-15-05 from PLX Inc., NY. Reflectivity per surface: 96 %  $\rightarrow$  88 % total reflectivity.

9. A. Beyer, L. Maisenbacher, K. Khabarova, A. Matveev, R. Pohl, Th. Udem, T. W. Hänsch, and N. Kolachevsky, "Precision spectroscopy of 2S-nP transitions in atomic hydrogen for a new determination of the Rydberg constant and the proton charge radius," *Phys. Scr.* **T165**, 014030 (2015).
10. W. He, Y. Fu, Y. Zheng, L. Zhang, J. Wang, Z. Liu, and J. Zheng, "Polarization properties of a corner-cube retroreflector with three-dimensional polarization ray-tracing calculus," *Appl. Opt.* **52**, 4527–4535 (2013).
11. H. Müller, S. W. Chiow, Q. Long, C. Vo, and S. Chu, "Active sub-Rayleigh alignment of parallel or antiparallel laser beams," *Opt. Lett.* **30**, 3323–3325 (2005).
12. S. Hannemann, E. J. Salumbides, and W. Ubachs, "Reducing the first-order Doppler shift in a Sagnac interferometer," *Opt. Lett.* **32**, 1381–1383 (2007).
13. Nufern S405 XP polarization maintaining fiber, mode field diameter MFD = 3.8 (5)  $\mu\text{m}$  ( $1/e^2$  intensity diameter, interpolated at 486 nm),  $w_0 = 1.9$  (25)  $\mu\text{m}$  ( $1/e$  field radius). AR coated by Diamond SA Via dei Patrizi 5, CH-6616 Losone.  $R \leq 0.1\%$ .
14. Combination of two cemented achromatic lens doublets from QIoptiq, G3222100000 ( $f = 80$  mm) and G32229000 ( $f = 40$  mm) equipped with AR coating ( $R \leq 0.1\%$ ).
15. E. G. Neumann, *Single Mode Fibers: Fundamentals* (Springer-Verlag, 1988).
16. Dielectric high reflecting mirror.  $R = 99.995\%$  at 486 nm. Custom made by Advanced Thin Films Boulder, CO.
17. A. E. Siegman, *Lasers* (University Science Books, 1986).
18. Thorlabs SM1Z translation mount.
19. QIoptiq Photonics GmbH & Co. KG, Königsallee 23, D-37081 Göttingen, Germany, <http://winlens.de/>
20. Lens-Optics GmbH, Bürgermeister-Neumeier-Strasse 7, D-85391 Allershausen, Germany. Custom made collimator ( $f=30$  mm) for wavelengths between 380 nm and 410 nm.
21. Mirror mount: Radiant Dyes Laser Accessories GmbH, MDI-H-2-1". Two Newport 8301-UHV piezomotor actuators have been installed in our lab.
22. N. Kolachevsky, J. Alnis, C. G. Parthey, A. Matveev, R. Landig, and T. W. Hänsch, "Low phase noise diode laser oscillator for 1S-2S spectroscopy in atomic hydrogen," *Opt. Lett.* **36**, 4299–4301 (2011).
23. J. Alnis, A. Matveev, N. Kolachevsky, Th. Udem and T. W. Hänsch, "Subhertz linewidth diode lasers by stabilization to vibrationally and thermally compensated ultralow-expansion glass Fabry-Perot cavities," *Phys. Rev. A* **77**, 053809 (2008).
24. C. G. Parthey, "Precision Spectroscopy on atomic hydrogen" (PhD thesis, Ludwig-Maximilians-Universität München, 2011).
25. A. Matveev, C. G. Parthey, K. Predehl, J. Alnis, A. Beyer, R. Holzwarth, T. Udem, T. Wilken, N. Kolachevsky, M. Abgrall, D. Rovera, Ch. Salomon, Ph. Laurent, G. Grosche, O. Terra, T. Legero, H. Schnatz, S. Weyers, B. Altschul, and T. W. Hänsch, "Precision measurement of the hydrogen 1S-2S frequency via a 920-km fiber link," *Phys. Rev. Lett.* **110**, 230801 (2013).
26. C. Cohen-Tannoudji, J. Dupont-Roc and G. Grynberg, *Atom - Photon Interactions: Basic Process and Applications* (Wiley-VCH Verlag GmbH, 2004).
27. F. Minardi, M. Artoni, P. Cancio, M. Inguscio, G. Giusfredi, and I. Carusotto, "Frequency shift in saturation spectroscopy induced by mechanical effects of light," *Phys. Rev. A* **60**(5), 4164–4167 (1999).
28. P. J. Mohr, B. N. Taylor, and D. B. Newell, "CODATA recommended values of the fundamental physical constants: 2010," *Rev. Mod. Phys.* **84**, 1527–1605 (2012).

## 1. Introduction

The Doppler effect can be a major obstacle in laser spectroscopy. It can lead to broadening of the observed resonances as well as a shift in their apparent line centers. The relative motion of atoms in a gas or in a beam gives rise to line broadening, while their center of mass motion shifts the line center. Laser cooling efficiently reduces both effects. Other techniques like fast collinear spectroscopy and supersonic expansion reduce only the relative motion and give rise to a narrow line width albeit with a large Doppler shift [1].

The first order Doppler shift of an individual atom moving at a velocity  $\vec{v}$  in a plane wave described by a wave vector  $\vec{k} = 2\pi/\lambda$  is given by

$$\Delta\nu_D = \frac{1}{2\pi} \vec{k} \cdot \vec{v} = \frac{v}{\lambda} \cos(\alpha), \quad (1)$$

where  $\lambda$  denotes the wavelength,  $v$  the magnitude of the atom's velocity vector and  $\alpha$  its angle with respect to the wave vector. Equation (1) expresses the first order Doppler shift in terms of wavefronts that the atom traverses per unit of time. It also suggests that instead of reducing the atomic velocity the first order Doppler effect may be canceled by arranging an atomic beam

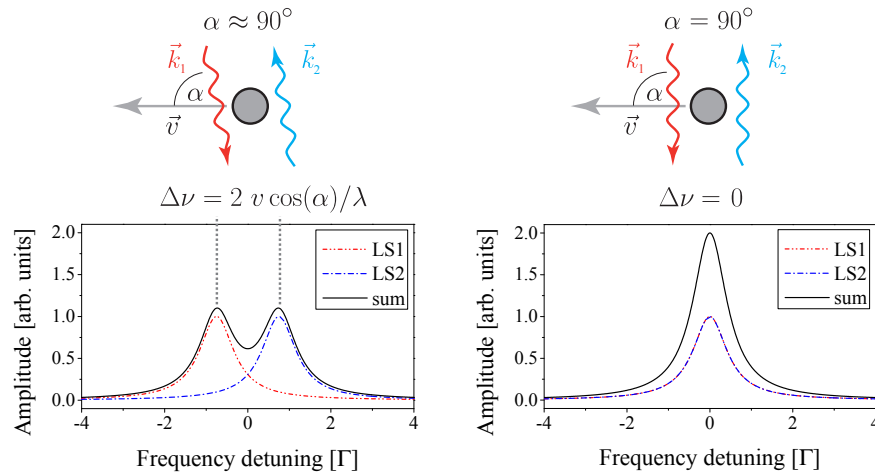


Fig. 1. Cancellation of the first order Doppler effect by utilizing counter-propagating laser beams. Left: counter-propagating laser beams at an angle different from  $\alpha = 90^\circ$  with respect to the atomic trajectory. The observed spectrum is a doublet with a separation  $\Delta\nu = 2v \cos(\alpha)/\lambda$ . The individual line shapes (LS1 and LS2) resulting from the interaction with one of the laser beams are indicated by dashed lines, the observed spectrum by a black solid line. The frequency detuning is measured in units of the natural line width  $\Gamma$ . Right: For an atom crossing the lasers at  $\alpha = 90^\circ$  the two components overlap. In either case the line center is unaffected provided that both laser beams have the same intensity. In practice one has to deal with curved wavefronts. Also in this case the average local first order Doppler effect vanishes provided that the wave fronts retrace each other, i.e. wave vectors  $\vec{k}_1$  and  $\vec{k}_2$  are anti-parallel at any given point.

perpendicular to the laser beam. However the requirements on alignment for a modern precision experiment are difficult to achieve in this way [2], in particular when the divergence of the atomic beam and the laser beam wave front curvature have to be taken into account.

A standard procedure to reduce this difficulty has been to employ two counter-propagating laser beams with  $\vec{k}_1 + \vec{k}_2 = 0$ , where  $\vec{k}_1$  and  $\vec{k}_2$  denote the respective wave vectors. This has been effective for several established Doppler-free methods like saturation spectroscopy [1] and two-photon spectroscopy [3]. In the latter case the Doppler shifts add to zero when an atom absorbs one photon from each of the two waves. For perfectly counter-propagating plane waves this compensation holds everywhere, independent of velocity. Neither a first order Doppler shift nor Doppler broadening takes place in this ideal situation so that the dominating effect becomes the much smaller second order Doppler effect [3] which will not be discussed here. In addition to the Doppler-free component, the two-photon transition amplitude comes with another component that is Doppler broadened [1]. This one is due to the absorption of two photons from either of the two waves.

Driving a one-photon dipole-allowed transition in a perfect standing wave of two exactly counter-propagating waves of equal intensity shows very similar features. In that case one obtains a doublet of symmetrically Doppler shifted spectral components, one for  $\vec{k}_1 \cdot \vec{v}$  (line shape LS1 in Fig. 1), the other for  $\vec{k}_2 \cdot \vec{v} = -\vec{k}_1 \cdot \vec{v}$  (line shape LS2 in Fig. 1). The center of weight of these components is free of the Doppler shift while the Doppler broadening manifests itself in terms of the separation of the two lines as sketched in Fig. 1.

While a two-photon transition is more immune to several imperfections, we demonstrate a method that allows approaching this ideal situation also with a one-photon dipole-allowed

transition. We experimentally determine an upper limit of the residual uncompensated Doppler shift by using atoms at different velocities. We find that residual uncompensated Doppler shifts are on average reduced to less than 4 parts in  $10^6$  of the full collinear shift in our setup which will be used for precision spectroscopy of the 2S-4P one-photon transition in atomic hydrogen at 486 nm. This transition could play a decisive role for the so-called “proton size puzzle” [4, 5], provided it can be measured with sufficient accuracy.

## 2. Corner cube retroreflectors and optical cavities

The common technique to generate anti-parallel waves is to reflect a laser beam using a corner cube retroreflector (see for instance [6, 7]). Two types are commercially available: prism type corner cubes and hollow retroreflectors. The latter can be manufactured with a specified maximum angular deviation of  $\varepsilon = 3$  rad [8], where  $\varepsilon$  is the angle between the incoming and the outgoing beams. Using Eq. (1), the residual uncompensated Doppler shift at angles  $\alpha$  close to 90 degree ( $\alpha = \pi/2 + \delta\alpha$ ) measured with respect to  $\vec{k}_1$ , can be written as:

$$\Delta\nu_{\text{resid}} = \frac{1}{2} \frac{v}{\lambda} [\sin(\delta\alpha) - \sin(\delta\alpha - \varepsilon)] \approx \frac{v}{2\lambda} \varepsilon. \quad (2)$$

In the last step, we have expanded the expression for small  $\delta\alpha$  and  $\varepsilon$  ( $\delta\alpha, \varepsilon \ll 1$  rad). It is important to note, that the right hand side of Eq. (2) is independent of  $\delta\alpha$  in first order, i.e. if no other imperfections are present, the residual Doppler effect is independent of the angle between the laser beams and the atomic beam. The small angular deviation  $\varepsilon$  rather leads to a constant offset, as is also depicted in Fig. 7 further below.

Reflecting the light off the three orthogonal surfaces of a corner cube retroreflector leads to wavefronts that are anti-parallel with high precision ( $\varepsilon = 3$  rad) and according to Eq. (2) would correspond to a residual uncompensated Doppler shift of 2 parts in  $10^6$  of the full collinear shift. However, the retroreflected beam is displaced laterally and its polarization is rotated. As a result atoms that cross the two beams in sequence might be optically pumped into a particular Zeeman sublevel in the first interaction zone and are then probed with a different polarization in the second zone. In addition, the polarization rotation significantly complicates the analysis of polarization dependent line distortions due to quantum interference [7, 9]. Illuminating the edges of the corner cube leads to wave front distortions [6], complicated polarization behavior [10] and attenuations that add to possible bulk and Fresnel losses. The latter reduces the amplitude of the spectral component that corresponds to the reflected beam. All of these effects give rise to asymmetric line distortions and hence to systematic shifts of the observed line center.

In order to circumvent these problems the two counter-propagating laser beams must have anti-parallel wave fronts such that  $\vec{k}_1 + \vec{k}_2$  vanishes everywhere. For a reflected Gaussian beam this means that its waist must be localized at the retroreflector and the latter must be at  $90^\circ$  relative to the laser beam axis. In addition, the local intensities of the two waves must be identical. For this the retroreflector should be highly reflective and wavefront distortions should be minimized. Corner cube retroreflectors may be used to achieve this goal when the laser beam is split into two arms. One contains the corner cube reflector to detect misalignments and the other one is used for precision spectroscopy [11].

An alternative to the use of a corner cube is the so-called “cat’s eye” configuration (see for instance Fig. 1 in [27]). Such a device may have good performance in terms of parallelism of the counter-propagating waves. Beam deviations of a few microradian may be possible using a 2f-configuration and lenses with focal lengths of tens of centimeters. However, the overlap of the two waves is not ensured and the additional lens introduces Fresnel and bulk losses. Even if the polarization is maintained, a partial overlapping of the beams can efficiently unbalance the fluorescence (sequentially) produced by each wave, similar to the case discussed for corner cubes above.



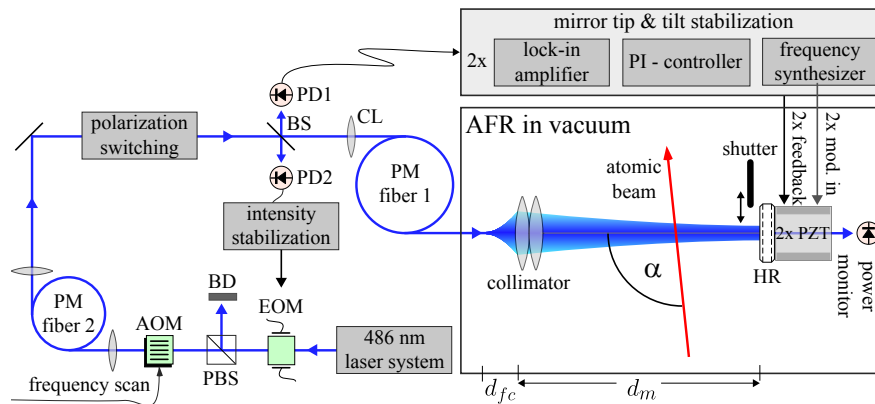


Fig. 2. Schematic view of the active fiber-based retroreflector (AFR). The main components are a polarization maintaining single mode optical fiber (PM fiber 1), a collimator with low imaging aberrations ( $f = 27$  mm) and an actively stabilized high reflectivity mirror (HR,  $R = 99.995\%$ ). The light emerging from fiber 1 is collimated such that the waist ( $w_0 = 2.1$  mm) is located on the flat HR mirror at a distance of  $d_m = 260$  mm. For an ideal Gaussian beam, this configuration leads to exactly retracing wave fronts. Deviations from this ideal situation may be due to spherical aberrations of the collimating lens. Experimentally this is verified by using an atomic beam with a variable mean velocity (see Sec. 6). Another polarization maintaining single mode fiber (PM fiber 2) is used as mode cleaner to improve reproducibility of the coupling efficiency to PM fiber 1. The latter may be affected by the settings of the acousto-optic modulator (AOM), the electro-optic modulator (EOM) and the laser operating conditions. PD: photo-detector, PZT: piezo-electric transducer, PBS: polarizing beam splitter, CL: coupling lens.

For deep-UV applications, where our AFR system may not readily be applied due to the lack of high quality optical single mode fibers, utilizing a Sagnac interferometer may represent an alternative in some cases [12]. However, it is important to note that small imbalances in the counter-propagating waves (i.e. imperfections of the beam splitter in the Sagnac interferometer) give rise to significant residual Doppler shifts as we discuss further below (see Eq. 7 in Sec. 4).

Another possibility that works in principle for all spectral regions from the IR to the deep UV would be to use a high finesse linear cavity. It has the advantage of enhancing the resonant, i.e. phase retracing mode, while at the same time attenuating possible mismatched waves. However, limiting the intra-cavity power  $P_{ic}$  to minimize excitation light power dependent systematic effects, such as the ac-Stark effect, optical pumping and saturation, means that an even lower power has to be coupled into the cavity and/or the finesse has to be restricted. Using some reasonable numbers for our 2S-4P experiment detailed in Sec. 6 ( $P_{ic} < 15$  W and beam waist  $w_0 \sim 2$  mm), one finds that it will be difficult to obtain a high quality error signal to stabilize a cavity with such a low power level. In principle, a second laser that is far detuned from resonance with the spectroscopy transition can be used to stabilize the cavity. Such a setup, however, would significantly increase the complexity of the system.

### 3. Active fiber-based retroreflector concept

In order to measure the absolute frequency of the 2S-4P transition in atomic hydrogen with an improved accuracy [2, 5, 9], we have constructed an active fiber-based retroreflector (AFR) as shown in Fig. 2. Light from a narrow-band continuous wave laser is coupled into a polarization maintaining single mode optical fiber (PM fiber 1 [13]). At the output of the fiber, inside the

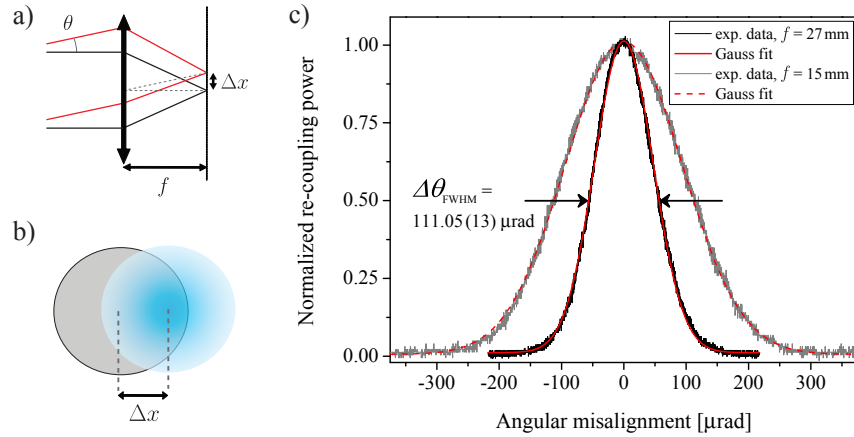


Fig. 3. Estimation of the alignment sensitivity of the active fiber-based retroreflector (AFR) shown in Fig. 2. a) Misalignment of the returning beam by an angle  $\theta$  leads to misplacement of the focus by  $\Delta x \approx \theta f$  and hence to a reduced re-coupling efficiency back into the single mode fiber. The convolution of the returning mode with the fiber mode as shown in b) gives  $\exp(-\Delta x^2/w_0^2)$  with a full width at half maximum of  $\Delta\theta_{\text{FWHM}} = 2w_0\sqrt{\ln(2)}/f$ . For  $f = 27\text{ mm}$  and  $w_0 = 1.90(25)\text{ }\mu\text{m}$  as specified [13] we obtain  $\Delta\theta_{\text{FWHM}} = 117(15)\text{ }\mu\text{rad}$ . c) Intensity measured at PD1 (Fig. 2) as a function of the returning beam angular misalignment (tilt). The misalignment is inferred from the applied PZT voltage and has been calibrated by measuring the beam deflection angle as a function of PZT voltage at a distance of 5 m. The response curve follows a Gaussian as expected and has a full width at half maximum of  $111.05(13)\text{ }\mu\text{rad}$ , in good agreement with the estimation using a) and b). For comparison the response curve of another collimator with  $f = 15\text{ mm}$  is shown (light gray). The reduced sensitivity to misalignment and the larger half width at half maximum of  $222.1(3)\text{ }\mu\text{rad}$  corresponds well to the reduction in focal distance.

vacuum chamber, the light is collimated with an objective of low imaging aberrations and a focal length of  $f = 27\text{ mm}$  [14]. The output of a step index fiber is very close to a Gaussian mode [15]. The objective position is chosen such that the waist of the collimated beam is located on the flat mirror (HR) with near unity reflectivity ( $R = 99.995\%$  [16]) that reflects the light back into the fiber. The fiber then serves as a small aperture converting angular misalignment of the returning beam into a measurable amplitude signal at photo detector PD1. Modulation of the HR mirror tip and tilt angles allows one to detect and correct misalignments using lock-in amplifiers (Sec. 5).

A simple estimate for the sensitivity to angular misalignment can be obtained using paraxial ray optics as illustrated in Fig. 3(a). Light incident on a thin lens under different angles is focused to different locations in the focal plane. Small angular misalignments result in a lateral displacement of the focused Gaussian beam with respect to the fiber mode. For the experimental implementation the measured full width at half maximum angle of the fiber re-coupling efficiency is found to be  $\Delta\theta_{\text{FWHM}} = 111.05(13)\text{ }\mu\text{rad}$ . The sensitivity can be increased by using collimation optics with larger focal lengths.

#### 4. Minimization of imperfections

This section discusses additional requirements that have to be fulfilled in order to minimize residual uncompensated Doppler shifts using the AFR. The first one is the use of a low imaging aberration collimator for good beam homogeneity and low phase distortions. Unfortunately these conditions mostly evade a simple quantitative analysis. However, one can get a qualitative picture

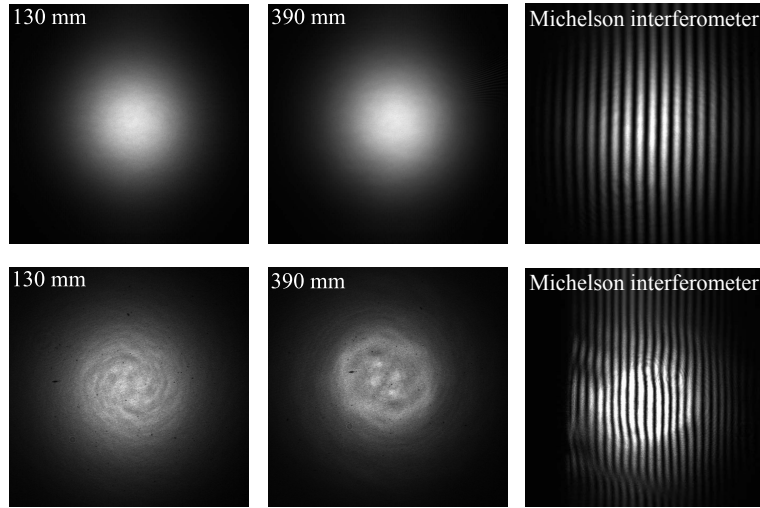


Fig. 4. Comparison of measured beam profiles for two different collimators tested for the active fiber based retroreflector (AFR). Upper row: collimator used in the current design (two achromatic lens doublets [14],  $f = 27$  mm). Bottom row: single aspheric lens ( $f = 30$  mm). Distances correspond to the intersection points of the forward (130 mm) and the backward (390 mm) traveling light with the atomic beam (see Fig. 2). Due to deviations from the ideal aspheric shape (surface roughness  $\approx 0.3$  m RMS), the beam profiles produced by the aspheric lens are not exactly Gaussian and the wave fronts do not exactly retrace each other. A slightly misaligned Michelson interferometer gives a qualitative estimate on the phase front distortions (right column).

by observing the transverse intensity profile of the collimated beam at various distances, as shown in Fig. 4 and Fig. 6. In principle, aspheric lenses can provide suitably small residual spherical aberration and minimize the number of reflecting surfaces in the beam path. Our experience, however, shows that this type of lenses is not necessarily a good choice depending on what kind of application they are optimized for and on the surface quality (Fig. 4).

In addition, the retracing of the wave fronts is influenced by the position of the beam waist, which in turn depends on the distance between the fiber tip and the rear principal plane of the collimating objective  $d_{fc}$  (see Fig. 2). Imaging of the Gaussian beam emerging from PM fiber 1 through the collimating objective to the mirror and back can be calculated using the standard matrix formalism for Gaussian beam propagation in optical systems [17]. The re-coupling losses  $L_{rc}$  for a certain distance  $d_{fc}$  and distance to the mirror  $d_m$  are given by the overlap integral of the focused returning beam with waist  $w_r$  and the fiber mode with waist  $w_0$ . Neglecting wave front curvature,  $L_{rc}$  can be approximated by:

$$L_{rc} \approx \frac{(w_0 - w_r)^2}{(w_0^2 + w_r^2)^2}, \quad (3)$$

where  $w_r$  is given by:

$$w_r = \frac{w_0}{f^2} \left[ \left[ 2d_{fc}d_m - 2(d_{fc} + d_m)f + f^2 \right]^2 + \left[ 2(d_{fc} - f)(d_{fc}d_m - (d_{fc} + d_m)f) \frac{\lambda}{\pi w_0^2} \right]^2 \right]^{1/2}. \quad (4)$$

For the collimator used in the experiment ( $f = 27$  mm), an axial displacement of only 15 m from the optimum position in  $d_{fc}$  results in a re-coupling loss of already 12%. Remote control

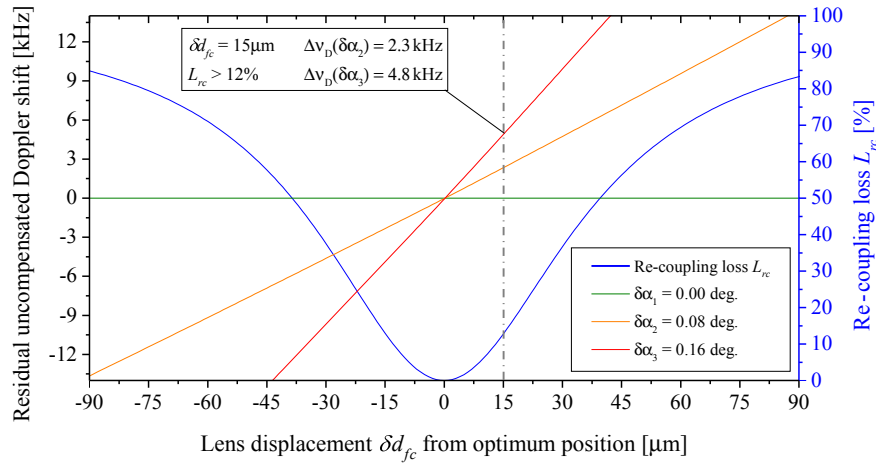


Fig. 5. Simulation of re-coupling losses (blue, right scale) and residual uncompensated Doppler shift (left scale) for an atom with velocity  $v = 300$  m/s as a function of the axial lens displacement  $\delta d_{fc}$  for an otherwise ideal active fiber-based retroreflector. The waist size of 2.1 mm in the simulation corresponds to the one determined for the lens assembly used in the current design (two achromatic lens doublets [14],  $f = 27$  mm). The Gaussian beams in forward and backward direction perfectly re-trace each other at  $\delta d_{fc} = 0$ , where the beam waist is located on the surface of the flat high reflecting mirror (Fig. 2). Atomic trajectories intersect the laser beams at angles  $\delta\alpha_1 = 0$  degree (green),  $\delta\alpha_2 = 0.08$  degree (orange) and  $\delta\alpha_3 = 0.16$  degree (red). If  $\delta d_{fc} = 0$ , Doppler shifts are perfectly canceled, independent of the laser-to-atomic-beam angle  $\alpha = \pi/2 + \delta\alpha$ . A small displacement of  $\delta d_{fc} = 15$  m (gray dashed line) results in a re-coupling loss of 12 % already, constituting a sensitive experimental handle on axial collimator misalignment.

of the distance  $d_{fc}$  is essential because the refractive index changes when the vacuum chamber housing the experiment is evacuated. If  $d_{fc}$  has been optimized in air and is not adjusted after evacuation, we measure a relative transmission loss of 46 % at PD1. A standard translation mount has been equipped with a remote-controlled piezo-actuator-driven micrometer screw to perform this task [18]. The axial position of the collimator  $d_{fc}$  is stable enough so that no active feedback is needed and occasional adjustments are sufficient.

The influence of displacements of the collimator from the optimum position in  $d_{fc}$  has been estimated based on a numerical simulation solving the optical Bloch equations for the hydrogen 2S-4P excitation discussed in section 6 and is shown in Fig. 5. We rewrite the Doppler shift in Eq. (1) using the parameter  $\eta(\delta\alpha)$  that measures the slope of the Doppler shift at an angle  $\alpha = 90^\circ \pm \delta\alpha$  as a function of atom velocity  $v$  in Hz/(m/s) or simply  $\text{m}^{-1}$ :

$$\Delta v_D = \eta(\delta\alpha) \times v, \quad (5)$$

where

$$\eta(\delta\alpha) = \frac{1}{\lambda} \times \sin(\delta\alpha). \quad (6)$$

Any first order Doppler shift is proportional to the atom velocity (Eq. (5)). The proportionality factor  $\eta$  can be expressed by Eq. (6) for plane waves or locally for any kind of wave front curvature. The definition in Eq. (5) will be used again in Sec. 6, where the slope  $\eta$  is studied experimentally. The residual uncompensated Doppler shift in the center of weight position extracted from the simulation for the collimator displacement of 15 m, i.e. re-coupling loss of

$L_{rc} > 12\%$ , and an otherwise ideal AFR system is approximately  $\eta_{cd}(0.08^\circ) \leq 7.7 \text{ m}^{-1}$ . At the thermal mean velocity  $\langle v \rangle = 300 \text{ m/s}$  of our sample atoms (cryogenic beam at 5.8 K, see Sec. 6), this corresponds to a residual shift of 2.3 kHz (Fig. 5). The measured re-coupling efficiency for the optimized system in the experiment, on the other hand, is found to be 100.4(9) % as discussed further below. With the high sensitivity to misalignment in  $d_{fc}$  brought by re-coupling losses, this uncompensated Doppler shift is well under control.

Imbalances in the intensities of the forward and backward traveling beams are largely suppressed by the use of an HR mirror ( $R = 99.995\%$  [16]) for retroreflection. The residual uncompensated Doppler shift can be estimated by approximating the resulting line shape by a sum of two Lorentzians with separation  $\Delta\nu = 2\nu \cos(\alpha)/\lambda$  as shown in Fig. 1. Assuming small excitation rates, i.e. saturation of the transition is negligible, imbalanced intensities transfer linearly to the respective amplitudes. For small deviations  $\delta\alpha$  and  $R \in [90\%; 100\%]$ , the uncompensated Doppler shift in the center of weight position can be approximated as a linear function of the intensity imbalance  $\xi = 1 - R$  if the separation of the two components is less than their line width:

$$\Delta\nu_{D,m} \approx \frac{v}{2\lambda} \times \delta\alpha \times \xi. \quad (7)$$

Note that in contrast to Eq. (2), the expression in Eq. (7) is linear in  $\delta\alpha$ , i.e. the corresponding uncompensated Doppler shift is no longer independent of the angle between the atomic and the laser beams. For our spectroscopy of the 2S-4P transition in atomic hydrogen, the estimate for the uncompensated shift due to intensity imbalance caused by the mirror reflectivity ( $\xi_m = 5 \times 10^{-5}$ ) amounts to only  $\eta_m < 0.23 \text{ m}^{-1}$  even for a large angle  $\delta\alpha = 0.5^\circ$ . In contrast to that, this effect is more than three orders of magnitude larger in the case of the aforementioned hollow corner cube retroreflector [8] with a specified  $\xi_{cc}$  of  $1.2 \times 10^{-1}$  and represents a strong limitation for using such a device directly in the spectroscopy beam path.

Residual imaging aberrations through the collimation optics, in particular spherical aberration and clipping, can cause aberrations in the wave fronts of the Gaussian beams. These deviations deform upon propagation and do not necessarily retrace in the returning beam as can be seen in the bottom row of Fig. 4 and middle row of Fig. 6. The lens system of the AFR presented here consists of a combination of two cemented achromatic lens doublets [14]. Although chromatic aberrations are irrelevant due to the use of a narrow-band laser, each individual lens doublet features a reasonably good compensation of the spherical aberration at the same time. Suitable combinations of doublets with low residual spherical aberration have been identified using the free software package WinLens Basic [19] and characterized using standard beam profiling techniques.

A slightly misaligned Michelson interferometer has been used to image wave front differences of the forward and backward traveling beams (Fig. 4). For the lens system presented in this text, no residual spherical aberration could be detected utilizing either technique.

We illustrate the importance of residual spherical aberration in Fig. 7 using a numerical simulation solving the optical Bloch equations for the hydrogen 2S-4P excitation (Sec. 6). The Doppler shift is exactly canceled for the ideal case of phase-retracing Gaussian beams. A small angular misalignment  $\epsilon$  between the forward and backward traveling beams results in a constant frequency offset according to Eq. (2). In the case shown,  $\epsilon$  equals 10 rad, a limit which can be beaten by our AFR as will be demonstrated in Sec. 6. Red triangles in Fig. 7 indicate the line centers obtained for the simulation data including spherical aberration as shown in the bottom row of Fig. 6.

Using “off-the-shelf” components represents a fast and cost-effective way to proceed. However, it turns out that the quality of the obtained beam profiles critically depends on the specific lenses used, even if they stem from the same production batch. Speckle patterns may be present, most probably caused by differences in the cementing process of the achromats. Therefore, we plan to use a multiplet of air-spaced spherical lenses for the next generation of the experiment



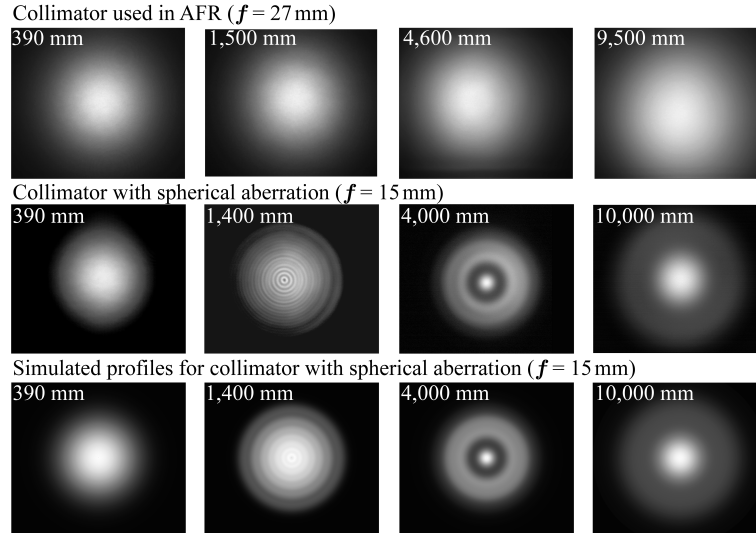


Fig. 6. Beam profiles acquired for the two collimators discussed in Fig. 3(c) (identical scale in all pictures). Both collimators produce acceptable beam profiles at moderate distances of up to 390 mm. The lens assembly used in the final design ( $f = 27$  mm [14]) produces a smooth Gaussian intensity profile even at a distance of 9.5 m (top row). In contrast to that, residual spherical aberrations cause significant radial intensity modulations at much smaller distances in case of the lens assembly used in a legacy version of our AFR ( $f = 15$  mm, middle row). The simulated beam profiles in the bottom row have been used for estimations of the residual uncompensated Doppler shift due to spherical aberrations in Fig. 7.

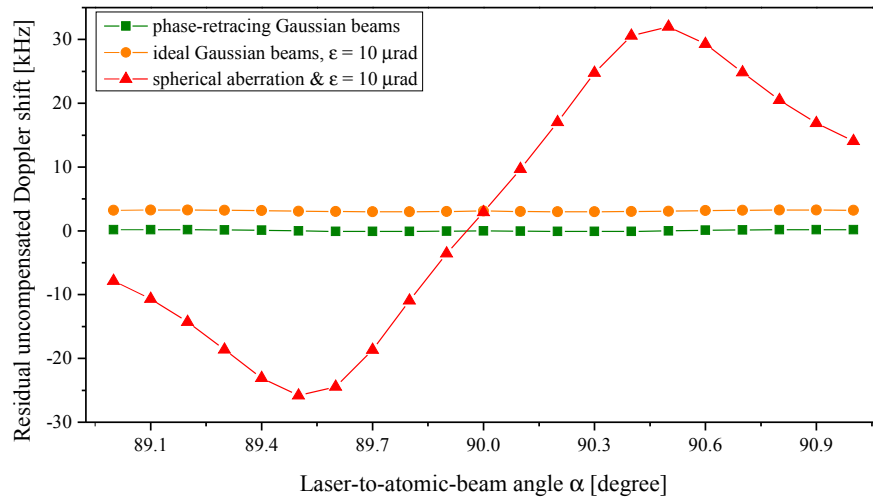


Fig. 7. Uncompensated residual Doppler shift for an atom traveling at  $v = 300$  m/s and different imperfections of the active fiber-based retroreflector (AFR). For an ideal AFR, the Doppler shift is compensated independent of the laser-to-atomic-beam angle  $\alpha$  (green squares). The case  $k_1 + k_2 \neq 0$  ( $\epsilon = 10$  rad for the case shown) for an otherwise ideal AFR leads to a constant shift of the observed resonance, where the offset is defined by Eq. (2) (orange circles). The presence of spherical aberrations (see simulated beam profiles in Fig. 6) leads to  $\alpha$ -dependent shifts of several tens of kilohertz (red triangles).

which is intended to probe the 2S-6P transition at 410 nm [20]. A total number of three individual lenses including one with negative focal distance is sufficient to compensate for spherical aberrations.

Another qualitative estimation for the proper implementation of the AFR can be obtained by measuring the amount of power that is coupled back into PM fiber 1. The re-coupling efficiency of an ideal AFR is unity (see Fig. 5). The re-coupling efficiency as defined by the overlap integral of the returning beam with the fiber mode cannot directly be measured in the experimental implementation. Instead, the power returning back through the fiber has to be measured after the beam splitter BS in Fig. 2. Losses due to different elements have to be considered in order to calculate the amount of power that has actually been coupled back into the fiber. In particular, these elements are the fiber end facets ( $R \leq 0.1\%$ ), the collimation objective of the AFR ( $R \leq 0.1\%$ ), the absorption of PM fiber 1 ( $A \leq 0.15$  dB), the collimation lens CL on the other end of PM fiber 1 ( $R \leq 0.5\%$ ), one additional mirror ( $R = 96.3(5)\%$ , not shown in Fig. 2) and the 50/50 beam splitter BS used to separate a fraction of the returning light ( $T = 50.3(5)\%$ ). Using these values, we infer a re-coupling efficiency of 100.4(9)% back into the fiber. This value should of course be smaller than 100% and we give a 90% confidence level lower limit of 99.0% re-coupling efficiency. At the given level of measurement accuracy, the re-coupling efficiency is indistinguishable from the 100% limit expected from an ideal AFR.

Light that is not mode matched with the fiber mode upon re-coupling, either due to a displacement of the collimator or residual imaging aberrations, is mostly scattered off the fiber ferrule. Since the fiber tip is cleaved at an angle of  $8^\circ$  and the distance to the spectroscopy region is sufficiently long (130 mm), the influence of the scattered light on the spectroscopy signal is expected to be small. In addition, proper anti-reflection coatings on all relevant optics, especially the collimator lenses [14] and the fiber end facets [13], suppress parasitic Fabry P  rot etalons. We tested for the latter by measuring the transmission of the HR mirror (power monitor, Fig. 2) and found no significant frequency dependence of the light intensity.

While certain imperfections listed in this section are hard to model, we can directly measure the corresponding residual uncompensated Doppler shifts in our spectroscopy experiment discussed in Sec. 6.

A PANDA type polarization maintaining (PM) fiber is used to provide a well defined polarization in our experiment. The fiber is equipped with stress rods in the cladding material that define the preferred PM fiber axes. The induced stress may also deform the fiber core, leading to slightly different beam diameters and shapes depending the input polarization. However, we do not see any significant influence of the input polarization on the residual Doppler shift and thus average data independent of the input polarization in Sec. 6.

## 5. Active stabilization

We use a dither method to stabilize the re-coupling into the fiber to its maximum value, i.e. maximize the retracing of the forward and backward traveling waves. The mount holding the HR mirror is equipped with two piezo actuator driven micrometer screws for coarse adjustment and two piezo actuators (PZTs) for fine adjustment and stabilization [21]. The PZT voltages are modulated by sine waves at frequencies of 1100 Hz and 876 Hz for tip and tilt, respectively, where we find acceptably small cross-talk between the two channels. Alternatively, a single modulation frequency and a  $90^\circ$  phase shift combined with a two-channel lock-in amplifier may be used [11].

The mirror tip and tilt angles were calibrated as a function of the PZT voltage by measuring the laser beam deflection for different voltages at a distance of about 5 m. In the linear regime of the PZT (below 50 V) the coefficient is found to be 9.9 rad/V in both directions and used to infer the angular beam misalignment in Fig. 3(c). The modulation amplitudes can be determined to be 1.0 rad and 0.4 rad, respectively, from the measured intensity modulation at PD1 and

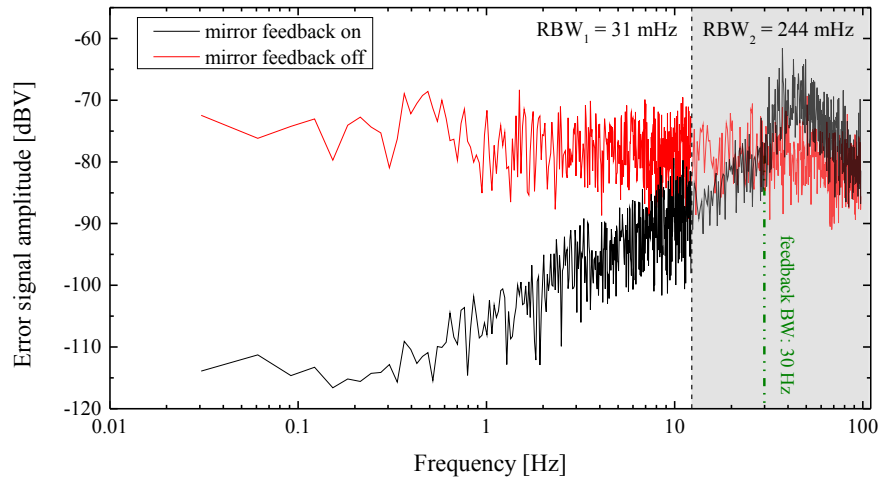


Fig. 8. FFT trace of the in-loop error signal produced by the lock-in amplifier in one of the AFR mirror feedback channels (tilt). The frequency interval [31 mHz; 12.2 Hz] has been recorded with a resolution band width ( $RBW_1$ ) of 31 mHz (left of black dashed line), for the interval [12.2 Hz; 97.4 Hz]  $RBW_2 = 244$  mHz (right of black dashed line). The difference in RBW has been accounted for by scaling the amplitudes measured in the second interval by the ratio  $RBW_1/RBW_2$ . The feedback bandwidth of 30 Hz (green dashed line) is determined by the crossing point of the noise figures in the stabilized (black) and unstabilized case (red). A servo bump is located at about 45 Hz.

using Fig. 3(c). These amplitudes correspond to a small Doppler shift of maximally 0.3 kHz at  $v = 300$  m/s, which is averaged to zero in our experiment due to the fact that the integration time of about 1 second in the data acquisition (Sec. 6) is much longer than the time scale of the modulation. The error signals for the PI-controllers in each channel (tip and tilt) are obtained by demodulation of the photo diode signal (PD1 in Fig. 2) using lock-in amplifiers ( $2\times$  Stanford Research Systems SR530). Since it is critical to maintain zero offset of the locking loop, a calibration of the lock-in amplifier and the PI-controller offsets should be performed. The input of the lock-in amplifier must be short-circuited or 50 Ohm terminated for this purpose while the reference frequency and settings are all maintained. The lock-in output is then fed into the error-input channel of the controller. Finally, with the P(I)-controller engaged (integrator off), the controller input offset is adjusted such that its output becomes zero. The AFR mirror feedback is optimized and characterized via the in-loop error signals after demodulation by the lock-in amplifiers. Figure 8 shows the FFT spectrum of the in-loop error signal in one of the channels (tilt) in the range between 31 mHz and 98 Hz. The feedback bandwidth is found to be about 30 Hz, indicated by the green dashed-dotted line at the crossing point of the noise figures in the stabilized and unstabilized case. The feedback servo bump is found at a frequency of 45 Hz. Measurements of the spectral noise figures in the second channel (tip) shows very similar results.

## 6. Suppression of the first order Doppler shift

The theoretical considerations in Sec. 4 give useful estimates for the performance of the AFR system. To thoroughly quantify the potential residual uncompensated Doppler shift, however, a direct measurement is required. To test the performance of the AFR we use our hydrogen spectrometer described in detail elsewhere [2, 9]. It makes use of a cold beam of metastable  $2S$  atoms that is generated via collinear laser excitation at 243 nm (not shown in Fig. 2). A beam

of ground state atoms emerges from a cold nozzle (5.8 K) and the Doppler-free two-photon excitation preserves the atoms' thermal velocity. The velocity distribution of 2S atoms is given by the product of the effusive Maxwellian velocity distribution of the ground state atoms at 5.8 K and the 1S-2S excitation probability. In combination with two diaphragms of 1.9 mm diameter (front) and 2 mm edge length (rear) separated by 109 mm, this results in a transverse velocity spread of less than 4 m/s (FWHM).

A perpendicular narrow-band continuous wave laser [22, 23] at 486 nm coupled to the AFR used in the experiment as shown in Fig. 2 excites the 2S-4P one photon transition. The sub-hertz laser line width is negligible compared to the 12.9 MHz natural line width of the atomic transition. The 4P state decays rapidly to the 1S ground state, emitting a photon at 97.2 nm (branching ratio 84 %). The 243 nm laser is periodically turned off by a chopper wheel running at 160 Hz (50% duty cycle) and subsequent 4P decays are detected in a time-of-flight resolved manner counting single photons with a multichannel scaler between 10 s and 2410 s after the 243 nm laser has been switched off. The experimentally observed line width is about 20 MHz, i.e. 1.5 times the natural line width, due to the atomic beam divergence (Doppler broadening) and power broadening, which contribute equally.

The distance from the hydrogen nozzle to the interaction region is  $d_{ni} = 165$  mm and the maximum velocity  $v_{\max}$  for atoms that arrive at a certain delay time  $\tau$  is given by the geometry  $v_{\max} = \tau/d_{ni}$ . The signal is grouped into 10 individual time windows (delays) and the velocity distributions in the individual time windows can be derived from Monte Carlo simulations as well as experimental data [3, 24]. The corresponding mean velocities range from about 270 m/s down to 70 m/s and slightly depend on experimental conditions.

To compare the situation with and without the Doppler suppression of the AFR, the returning laser beam can be periodically blocked by a shutter depicted in Fig. 2. The atomic resonance is scanned in random order and at each frequency point, two sets of data are acquired. For one set the shutter is open, i.e. the AFR is active, and for the second one the shutter is closed and only one beam interacts with the atomic sample. This type of differential measurement offers a high degree of common noise suppression for other systematic effects that vary on a time scale longer than the data acquisition time of about 3 seconds per laser frequency setting. The fiber, collimation optics and HR mirror of the AFR are fixed to a rotatable mount inside the vacuum chamber (not shown in Fig. 2). The angle  $\alpha$  between the laser beams and the atomic beam can be adjusted remotely by rotating the AFR axis with respect to the atomic beam. The angle  $\alpha$  can be read from a vernier scale inside the vacuum chamber. We find the position of  $\alpha = 90^\circ$  by measuring resonances with one laser beam only (shutter closed, similar to red data in Fig. 9) at different angle settings. The position of  $\alpha = 90^\circ$  on the vernier scale is found by interpolation to the point of zero slope ( $\eta = 0 \text{ m}^{-1}$ ) with an uncertainty smaller than  $0.01^\circ$  after about 30 minutes of data acquisition. Alternatively, albeit with reduced sensitivity, the alignment may be determined by measuring the observed line width as a function of the laser-to-atomic-beam angle [6]. The angle  $\alpha = 90^\circ$  can be set with an uncertainty of  $0.08^\circ$  and is limited by the read-off accuracy of a vernier scale.

500 pairs of 2S-4P resonances (shutter open and closed) have been recorded for this demonstration in about 4 hours of data acquisition time. For small deviations from  $\alpha = 90^\circ$ , the atomic spectra can be fit with Voigt functions to measure the uncompensated Doppler shift. Mean values of the extracted line centers are shown in Fig. 9 as a function of the mean velocity  $\langle v \rangle$  of atoms contributing to the corresponding delayed signals. The observed slopes  $\eta$  are limited by statistics and compatible with zero if the AFR is active. The angle  $\alpha_{\text{exp}} = 89.60^\circ \pm 0.03^\circ$  extracted from the experimental data using only one laser beam (red circles) is compatible with the less accurate mechanical reading of the vernier scale and shows that the adjustment is reproducible with sufficient accuracy. Due to its large sensitivity to the Doppler shift, the data with the Doppler cancellation switched off is a suitable tool for the determination of  $\alpha$ , however

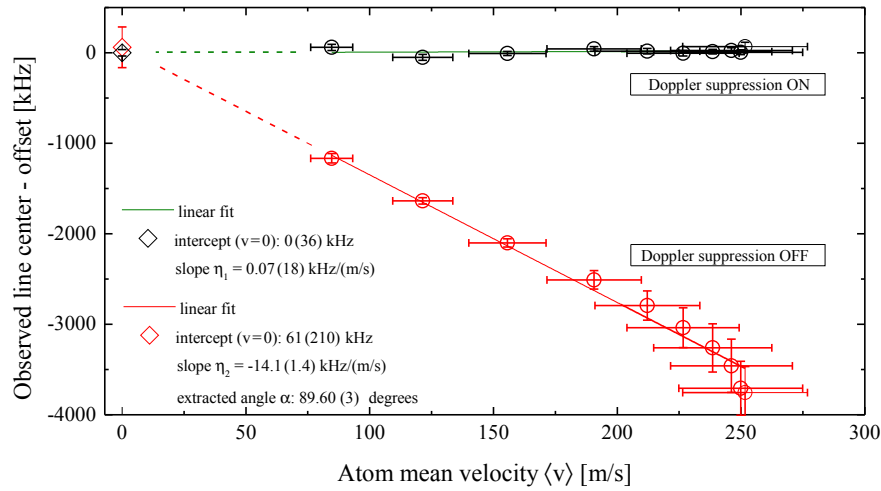


Fig. 9. Observed transition frequency in the lab frame with and without Doppler suppression. Imperfections of the active fiber-based retroreflector are characterized by a differential measurement of the 2S-4P transition at an angle of  $\alpha = 89.60^\circ \pm 0.03^\circ$  ( $\alpha$  as defined in Fig. 2, 4 hours of data acquisition). Red circles: Doppler suppression off, i.e. the shutter in Fig. 2 is closed. Black circles: Doppler suppression active, i.e. shutter open. Experimental uncertainties for the latter case are small on this scale and shown inside the open circles. For better readability, the frequency axis is offset by  $\approx 616$  THz such that the linear fit of the black data extrapolates to zero at  $v = 0$ . The observed slope  $\eta_1$  (Doppler suppression on) of the extracted transition frequency as a function of atom mean velocity  $\langle v \rangle$  is limited by statistics and compatible with zero. Due to its large sensitivity to the Doppler shift ( $\eta_2 = 14.1(1.4)$  kHz/(m/s)), the data with the Doppler cancellation switched off is a suitable tool for the determination of  $\alpha$ , however not for precision spectroscopy at an accuracy level of a few tens of kilohertz, i.e. a few parts in  $10^5$  of the full collinear Doppler shift. Still, intercepts at  $v = 0$  of the two data sets coincide within the given uncertainties.

not for precision spectroscopy at an accuracy level of a few tens of kHz, i.e. a few parts in  $10^5$  of the full collinear Doppler shift. Still, the intercepts at  $v = 0$  of the two data sets agree, indicating internal consistency of the analysis.

According to Eq. (1) and Eq. (2) the Doppler shift for blocking and unblocking the back reflected laser beam is given by  $\delta\alpha \times v/\lambda$  and  $\epsilon \times v/2\lambda$ , respectively. Typically the deviation  $\delta\alpha$  from perfect perpendicular alignment between the atomic and the laser beams is much larger than the angle between the forward and backward traveling laser beam  $\epsilon$ . A comparison between the two situations does not give a reliable estimate for  $\epsilon$ . Unfortunately this is the angle that is required to estimate the residual first order Doppler shift. Therefore we directly measure the residual uncompensated Doppler shift in a long term measurement.

In 15 days of measurement, distributed over one month of run time, a total number of 48,000 individual resonances of the 2S-4P transition have been acquired. The data set has been acquired with the AFR suppressing the Doppler shift, similar to the black data shown in Fig. 9. The angle between the atomic beam and the laser beams has been adjusted to  $\alpha = 90^\circ \pm 0.08^\circ$  using the same procedure described above. As before, we use our time-of-flight resolved detection scheme to obtain 2S-4P line centers as a function of the mean velocity  $\langle v \rangle$  of atoms contributing to the signal. Average values of the residual uncompensated Doppler shift slopes  $\eta_j$  are shown in Fig. 10 for each measurement day. Uncertainties for the mean values per measurement day are approximately  $35 \text{ m}^{-1}$ . For comparison, the expected slope using only one laser beam at an angle



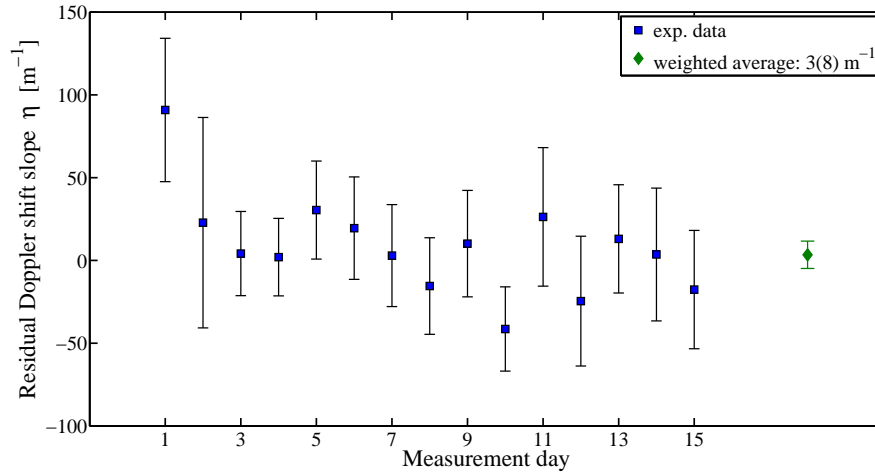


Fig. 10. Characterization of residual uncompensated first order Doppler shift. The angle between the atomic beam and the counter-propagating laser beams provided by the active fiber-based retroreflector (AFR) is adjusted to  $\alpha = 90^\circ \pm 0.08^\circ$ . Line centers of the 2S-4P transition in atomic hydrogen have been extracted from a total number of 48,000 resonance profiles as a function of the mean velocity of the atoms contributing to the respective signal. Blue data points indicate average values of the residual uncompensated Doppler shift slope  $\eta_j$  per measurement day and active AFR (similar to black data in Fig. 9). Average uncertainties per day amount to about  $35 \text{ m}^{-1}$ . No excessive scatter of the experimental data is observed and we determine the overall average to be  $\eta_{\text{exp}} = 3(8) \text{ m}^{-1}$ . This limit corresponds to a reduction of the collinear Doppler shift  $\eta(90^\circ) = 2.05 \times 10^6 \text{ m}^{-1}$  to less than 4 parts in  $10^6$ .

of  $89.92^\circ$  is  $2871 \text{ m}^{-1}$ . No excessive scatter of the experimental data is observed ( $\chi^2/\text{dof} = 0.72$ ,  $\text{dof} = 14$ ) and we determine the overall average to be  $3 \pm 8 \text{ m}^{-1}$ . This measurement of the uncompensated Doppler shift is compatible with zero and includes all possible imperfections of the Doppler compensation using our AFR as discussed above. Compared to the full Doppler shift of  $\eta(90^\circ) = 2.05 \times 10^6 \text{ m}^{-1}$ , this limit corresponds to a reduction to less than 4 parts in  $10^6$ .

The corresponding Doppler shifts amount to  $\Delta\nu_D = 0.8(2.2) \text{ kHz}$  for the fastest of our velocity classes ( $\langle v \rangle \approx 270 \text{ m/s}$ ) and  $\Delta\nu_D = 0.20(56) \text{ kHz}$  for the slowest ( $\langle v \rangle \approx 70 \text{ m/s}$ ). Assuming a residual uncompensated Doppler shift of the observed size was solely caused by an angular mismatch of the returning beam of an otherwise ideal AFR, the corresponding misalignment amounts to  $\epsilon_{\text{AFR}} = 2.9(7.7) \text{ rad}$ . Note that this value corresponds to the overall average over more than four weeks of data taking. While it does not necessarily mean that possible angular deviations are smaller than this value at any given time, opening the vacuum chamber every second day of measurement for maintenance, readjustments in the apparatus and changing of experimental conditions (in particular laser powers and polarization) neither lead to excessive scatter nor to a significant residual uncompensated Doppler shift over this long period of time. In addition, this value of  $\epsilon_{\text{AFR}}$  also incorporates all other possible imperfections of the system and therefore represents an upper limit for the average misalignment of the returning beam.

## 7. Line distortions due to the coherent interaction with two laser beams

While the atoms cross the interaction region, they interact coherently with both laser beams forming the standing wave. The absorption and stimulated emission from and into these beams and the associated change in momentum can lead to a multitude of effects, possibly distorting

the fluorescence line shape. In some situations, however not in our particular system as detailed below, this can be described as the well-known dipole and recoil force acting on localized atoms [26]. In this approximation, atoms are attracted by the nodes or antinodes for a red or blue detuned laser, leading to asymmetric light-force induced line distortions and systematic frequency shifts. This mechanism has been described before and was identified as the leading systematic effect of optical spectroscopy of the helium  $2^3S_1 \rightarrow 2^3P_{0,1,2}$  transitions [27]. Such effects, if present, could potentially mask the verification of the Doppler cancellation shown in Fig. 9 and Fig. 10.

Treating the external motion classically and the internal degrees of freedom quantum mechanically works only under several conditions [26]. One of them is that the atoms stay well localized on a length scale much smaller than the periodicity of the standing wave, i.e.  $\lambda/2$ . This condition is indeed fulfilled for the helium  $2^3S_1 \rightarrow 2^3P_{0,1,2}$  transition. However, for our 2S-4P setup this is not the case because of the lower mass, the larger photon momentum, the smaller scale size of the standing wave and the longer interaction time in the laser field. The recoil of a single photon due to the internal superposition of the 2S and the 4P state would generate two distinct classical trajectories that separate by several  $\lambda/2$  upon propagation through the laser beam.

To model the interaction with the two laser beams in this regime the external degrees of freedom of the atoms have to be described by wave mechanics. In this picture coherent superpositions of the momentum eigenstates are generated by the back decay to the 2S state. The corresponding two photon recoil gives rise to a small spatial modulation of the atomic density with a period of  $\lambda/2$ , that either lines up with the nodes or antinodes of the laser field. Again, this process depends on the laser detuning, giving rise to line shape distortions. In our system, the 4P atoms predominantly decay to the 1S ground state due to the favorable branching ratio and only 4% of the atoms return to the initial hyperfine 2S sub-level ( $F = 0$ ). This largely suppresses the spatial modulation of the atomic density. We have set up a model that describes our system in the quantum regime and found that the corresponding line shifts are negligible for the purpose of this work. The details are subject to an upcoming publication.

## 8. Conclusions

We have shown that our active fiber-based retroreflector is capable of providing high quality phase-retracing anti-parallel laser beams of equal intensity for the suppression of Doppler shifts in precision spectroscopy experiments. Possible residual uncompensated Doppler shifts have been limited experimentally to be smaller than 4 parts in  $10^6$  of the full collinear shift on average. The AFR system is easy to build and operate. Its modular design makes it scalable as well as applicable to a wide range of wavelengths and experimental applications where alternative techniques using optical cavities or corner cube retroreflectors may not be the most favorable choice.

We plan to use the AFR for a measurement of the 2S-4P absolute transition frequency in atomic hydrogen. Combining the result with the 1S-2S transition frequency also measured in our lab [3, 25], the Rydberg constant and the proton charge radius can be determined simultaneously. Today, the most precise determinations of these parameters from atomic hydrogen stem from measurements of 2S- $nL$  ( $n = 6, 8, 12$ ,  $L = S, D$ ) two photon transition frequencies (see references in [28]). The reduction of the Doppler shift demonstrated here, combined with spectroscopy on a cold beam of hydrogen atoms is large enough to enable measurements with competitive accuracy using 2S- $nP$  transitions instead [2, 9].

## Funding

Deutsche Forschungsgemeinschaft (DFG) (HA 1457/101-1), European Research Council (ERC) (Starting Grant #279765), European Union integrated project SIQS, Max-Planck-Foundation, Russian Science Foundation (RSF) (16-12-00096).